

Systematics of toroidal dipole modes in Ca, Ni, Zr, and Sn isotopes

A. Repko¹, V.O. Nesterenko^{2,3,4}, J. Kvasil⁵, and P.-G. Reinhard⁶

¹ Institute of Physics, Slovak Academy of Sciences, 84511 Bratislava, Slovakia

² Laboratory of Theoretical Physics, Joint Institute for Nuclear Research, Dubna, Moscow Region, 141980, Russia

³ State University "Dubna", Dubna, Moscow Region, 141980, Russia

⁴ Moscow Institute of Physics and Technology, Dolgoprudny, Moscow region, 141701, Russia

⁵ Institute of Particle and Nuclear Physics, Charles University, CZ-18000 Prague 8, Czech Republic

⁶ Institut für Theoretische Physik II, Universität Erlangen, D-91058, Erlangen, Germany

Received: date / Revised version: date

Abstract. We analyze the relation between isoscalar toroidal modes and so-called pygmy dipole resonance (PDR), which both appear in the same region of low-energy dipole excitations. To this end, we use a theoretical description within the fully self-consistent Skyrme quasiparticle random-phase approximation (QRPA). Test cases are spherical nuclei: $^{40,48}\text{Ca}$, $^{58,72}\text{Ni}$, $^{90,100}\text{Zr}$, and $^{100,120,132}\text{Sn}$ which cover four different elements and for each element at least two isotopes with different neutron excess, one small and another large. The structure of the modes is investigated in terms of strength functions, transition densities (TD) and transition currents (TC). For all considered nuclei, we see that, independently on whether PDR strength exists or not, the flow pattern in the lower part of the "PDR energy region" is basically an isoscalar vortical toroidal motion with a minor irrotational fraction. A one-to-one correspondence between calculated TD and TC is established. The toroidal flow appears already in the uncoupled two-quasiparticle (2qp) excitations and becomes definitively strong for the QRPA modes. Altogether, we find that low-lying dipole strength often denoted as isoscalar PDR is actually an oversimplified imitation of the basically toroidal motion in nuclei with sufficient neutron excess.

PACS. XX.XX.XX No PACS code given

1 Introduction

The dipole toroidal mode in nuclei represents a remarkable example of confined vortical flow [1, 2, 3]. This mode forms a vortical ring, called a Hills vortex in hydrodynamics [4, 5]. In 1983, S.F. Semenko has predicted the existence of a toroidal dipole resonance (TDR) in nuclei located at an energy $E \approx (50 - 70)A^{-1/3}$ MeV [1]. During subsequent decades, TDR was a subject of intense theoretical studies both in macroscopic and self-consistent microscopic models, see e.g. [6, 7, 8, 9, 10, 11, 12] and more references in the reviews [2, 3]. There are numerous experimental data from isoscalar (α, α) scattering [13, 14, 15, 16, 17, 18, 19] and nuclear fluorescence [20] which claim that TDR forms the low-energy part of the isoscalar giant dipole resonance (IS GDR) while the high-energy part of IS GDR is ascribed to the irrotational compression dipole resonance (CDR), for reviews see [2, 21]. Schematic vortical TDR and irrotational CDR velocity fields are shown in Fig. 1. However, despite impressive theoretical and experimental efforts, some important features of the TDR are still under debate and its unambiguous experimental observation has yet to come, see e.g. the discussion in [22].

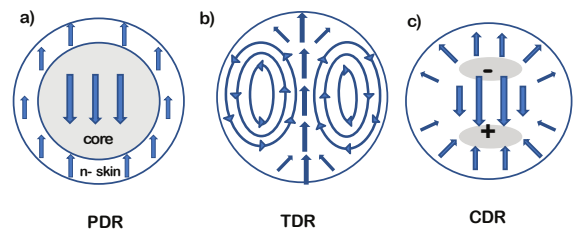


Fig. 1. Sketch of velocity fields for PDR (a), TDR (b) and CDR (c) flows. The arrows indicate direction (not strength) of the flows. In the plot (c), compression (+) and decompression (-) regions with increased and decreased densities are marked.

During last decade, our collaboration studied continuously various features of the vortical dipole toroidal mode [3, 22, 23, 24, 25, 26, 27, 28, 29, 30, 31] using separable [32, 33] and non-separable [22, 34] versions of the fully self-consistent Quasiparticle Random Phase Approximation (QRPA) approach with Skyrme forces. The key observables of the

TDR, namely strength functions, transition densities (TD), and transition current (TC), were analyzed in spherical and deformed nuclei. TDR and CDR were analyzed with respect to the familiar criteria of nuclear vorticity [26]. A new route in exploration of the vortical toroidal mode in nuclei was recently proposed [29,30]. It was shown that there should exist low-lying individual toroidal dipole states well separated from neighboring excitations in light axially-deformed nuclei. These states can be easier observed and identified than in the swamp of low-energy modes in heavier nuclei. Similar results for light nuclei were obtained within the approaches involving cluster degrees of freedom [35,36,37,38,39].

The present study will concentrate in one of the most interesting and significant aspects concerning the toroidal mode: the relation between isoscalar TDR and low-energy part of so called pygmy dipole resonance (PDR). It is known that PDR is split into the low-lying isoscalar (IS) fraction, often interpreted by neutron-skin oscillations, and a higher isovector (IV) part [40,41,42]. The TDR also has IS and IV components [23]. As shown in our previous works [3,24,25], the IS PDR can be viewed as a local manifestation of the IS toroidal mode on the nuclear surface showing up in nuclei with sufficient neutron excess ($N > Z$). Indeed, IS TDR and PDR lie in the same energy region and our calculated current distributions for dipole states in the IS PDR region show clear toroidal pattern [3, 24, 25] schematically illustrated in plot (b) of Fig. 1. Besides, the analysis of strength functions and TD indicates that dipole states in the IS PDR region also have a minor compressional fraction [23,24,43]. While the TC is dominated by vortical toroidal flow, the TD is perhaps mainly determined by the irrotational compressional fraction. For the latter, see also results of the correlation analysis [43].

Our previous analysis of the relation between IS TDR and PDR was performed only for a few selected nuclei: ^{120}Sn [3], ^{208}Pb [24,25], and ^{154}Sm [22]. Here we aim at a more systematic survey and extend our exploration to a wider set of nuclei, namely to Ca, Ni, Zr and Sn isotopes ($40 \leq A \leq 132$). For each element, isotopes with and without neutron excess will be compared. Our goal is to show that low-energy dipole spectra in all considered nuclei, independently of their neutron excess, represent predominantly the toroidal current distribution with some irrotational fractions and that, in nuclei with $N > Z$, this flow appears also as PDR peaks. We will demonstrate that the neutron flow at the nuclear boundary can be roughly imitated by a PDR-like irrotational pattern, see panel (a) in Fig. 1. Note that our study addresses only IS parts of TDR and PDR. Following [23], the IV TDR pattern is more complicated and its comparison with IV PDR requires a separate analysis.

The paper is organized as follows: In Section 2, the theoretical and calculation background is sketched. In Sec. 3, results of the calculations for Ca, Ni, Zr, and Sn isotopes are discussed. The low-energy dipole spectrum in ^{120}Sn is scrutinized in most detail. In Sec. 4, the features of TDR and PDR are compared and possible reactions for observation of the vortical toroidal mode are briefly discussed.

Conclusions are given in Sec. 5. Appendix A includes definitions of the density and current operators with the relevant effective charges. In Appendix B, the calculated and observed dipole strengths in ^{120}Sn are compared. A list of acronyms is provided in Appendix C.

2 Theoretical and calculation background

The calculations are performed within QRPA [44] based on the Skyrme energy functional [45,46]

$$\mathcal{E}(\rho, \tau, \mathbf{J}, \mathbf{j}, \mathbf{s}, \mathbf{T}, \tilde{\rho}) = \mathcal{E}_{\text{kin}} + \mathcal{E}_{\text{Sk}} + \mathcal{E}_{\text{Coul}} + \mathcal{E}_{\text{pair}} \quad (1)$$

including kinetic, Skyrme, Coulomb and pairing parts. The Skyrme part \mathcal{E}_{Sk} depends on the following local densities and currents: density $\rho(\mathbf{r})$, kinetic-energy density $\tau(\mathbf{r})$, spin-orbit density $\mathbf{J}(\mathbf{r})$, current $\mathbf{j}(\mathbf{r})$, spin density $\mathbf{s}(\mathbf{r})$, and spin kinetic-energy density $\mathbf{T}(\mathbf{r})$. The Coulomb part includes direct and exchange term, the latter is treated in Slater approximation. The pairing functional depending on the pairing density $\tilde{\rho}(\mathbf{r})$ is derived from a zero-range contact interaction [47]. Here we use mainly volume pairing (without dependence on density $\rho(\mathbf{r})$) treated at the BCS level [22].

The mean-field Hamiltonian and QRPA residual interaction are determined through the first and second functional derivatives of the total energy (1), see e.g. [48]. We do not employ the separable ansatz for the residual interaction, as done in earlier papers [23,34], but use full QRPA solved as matrix equations in configuration space. The approach is fully self-consistent since: i) both the mean field and residual interaction are obtained from the same Skyrme functional, ii) time-even and time-odd densities are used, iii) the residual interaction includes all the terms of the initial Skyrme functional as well as the Coulomb direct and exchange terms, iv) both ph- and pp-channels in the residual interaction are taken into account.

Most calculations are performed with the Skyrme force SLy6 [49]. Earlier, this force was successfully used for the systematic exploration of IV-GDR in rare-earth, actinide and superheavy nuclei [50]. Since our study is mainly applied to dipole excitations, we continue to use SLy6. To check the dependence of our results on Skyrme parametrizations, we counter check the case with ^{120}Sn using the forces SV-bas [51] and SkM* [52]. SLy6 and SkM* calculations are performed with the simple volume pairing. SV-bas is defined with surface pairing and so that is used in this particular case.

We employ a large two-quasiparticle (2qp) basis ranging up to 120 MeV in ^{120}Sn . With this basis, the Thomas-Reiche-Kuhn sum rule [44,53] and isoscalar energy-weighted sum rule [21] are exhausted by 99 - 103 %.

The relevant characteristics for our analysis are strength functions, transition densities, and current transition densities. The strength function for $E1$ transitions between

QRPA ground state $|0\rangle$ and excited state $|\nu\rangle$ reads

$$S_X(E1, T; E) = \sum_{\mu \geq 0} (2 - \delta_{\mu,0}) \quad (2)$$

$$\cdot \sum_{\nu} [E_{\nu}]^{m_X} |\langle \nu | \hat{M}_{1\mu}^X(T) | 0 \rangle|^2 \xi_{\Delta}(E - E_{\nu})$$

where E is the excitation energy, $\hat{M}_{1\mu}^X(T)$ is the transition operator, μ is its azimuthal angular momentum, $X = \{\text{el, com, tor}\}$ marks the type of the excitation (isovector $E1(T=1)$, compressional isoscalar $E1(T=0)$, toroidal isoscalar $E1(T=0)$), E_{ν} is the energy of the QRPA state. We have the energy factor ($m_X=1$) for $X = \text{el}$ and no factor ($m_X=0$) for $X = \text{com, tor}$. The effective charges for transition operators $\hat{M}_{1\mu}^X(T)$ are given in Appendix A.

The strength function is weighted by a Lorentz function

$$\xi_{\Delta}(E - E_{\nu}) = \frac{1}{2\pi} \frac{\Delta(E)}{(E - E_{\nu})^2 + [\Delta(E)/2]^2} \quad (3)$$

with energy-dependent folding [27]

$$\Delta(E) = \begin{cases} \Delta_0 & \text{for } E \leq E_0, \\ \Delta_0 + a(E - E_0) & \text{for } E > E_0. \end{cases} \quad (4)$$

The Lorentzian folding with $\xi_{\Delta}(E - E_{\nu})$ is used to simulate the escape width and the coupling to the complex configurations (spreading width). Since these two effects grow with increasing excitation energy, we employ an energy dependent folding width $\Delta(E)$ with the parameters $\Delta_0=0.3$ MeV, $E_0 = \min\{S_n, S_p\}$ MeV (with S_n and S_p being neutron and proton separation energies) and $a=0.1667$ [22].

The IV dipole operator ($X = \text{el}$) reads

$$\hat{M}_{1\mu}^{\text{el}}(T=1) = e \sum_{q=n,p} e_{\text{eff}}^q \sum_{i \in q} r_i Y_{1\mu}(\Omega_i) \quad (5)$$

where $Y_{1\mu}(\Omega_i)$ is the spherical harmonic and e_{eff}^q are effective charges equal to N/A for protons ($q=p$) and $-Z/A$ for neutrons ($q=n$). For this operator, the photoabsorption is

$$\sigma_{\gamma}(E1, T=1; E) = 0.402 S_{\text{el}}(E1, T=1; E) [\text{fm}^2]. \quad (6)$$

The toroidal IS dipole operator reads [23]

$$\hat{M}_{1\mu}^{\text{tor}}(T=0) = -\frac{1}{10c\sqrt{2}} \int dr r^3 \mathbf{Y}_{11\mu}(\Omega_i) \cdot (\nabla \times \hat{\mathbf{j}}_{\text{nuc}})$$

$$= -i \frac{1}{2c\sqrt{3}} \int dr \hat{\mathbf{j}}_{\text{nuc}}$$

$$\cdot \left[\frac{\sqrt{2}}{5} r^2 \mathbf{Y}_{12\mu}(\Omega) + (r^2 - \langle r^2 \rangle_0) \mathbf{Y}_{10\mu}(\Omega) \right] \quad (7)$$

where $\hat{\mathbf{j}}_{\text{nuc}}(\mathbf{r}) = \hat{\mathbf{j}}_{\text{c}}(\mathbf{r}) + \hat{\mathbf{j}}_{\text{m}}(\mathbf{r})$ is the operator of nuclear current including convective and magnetization parts, see the explicit expression in the Appendix A, and $\mathbf{Y}_{10\mu}(\Omega)$ and $\mathbf{Y}_{12\mu}(\Omega)$ are vector spherical harmonics. The terms with the ground-state square radius $\langle r^2 \rangle_0$ take care of the center-of-mass corrections [21, 23, 31]. The toroidal operator (7) is formally a sum of vortical and irrotational

(compressional) parts [23, 26]. However, the low-energy response (2) from this operator is mainly vortical [23, 26].

The operator for IS compressional dipole can be written in terms of the nuclear current [21, 23],

$$\hat{M}_{1\mu}^{\text{com}}(T=0) = -i \frac{1}{10c} \int dr r^3 Y_{1\mu}(\Omega) (\nabla \cdot \hat{\mathbf{j}}_{\text{nuc}})$$

$$= -i \frac{1}{2c\sqrt{3}} \int dr \hat{\mathbf{j}}_{\text{nuc}}$$

$$\cdot \left[\frac{2\sqrt{2}}{5} r^2 \mathbf{Y}_{12\mu}(\Omega) - (r^2 - \langle r^2 \rangle_0) \mathbf{Y}_{10\mu}(\Omega) \right], \quad (8)$$

or, using the continuity equation, in the familiar form

$$\hat{M}_{1\mu}^{\text{com}}(T=0) = \frac{e}{20} \sum_{i=1}^A [r_i^3 - \frac{5}{3} \langle r^2 \rangle_0 r_i] Y_{1\mu}(\Omega_i). \quad (9)$$

The compressional operator is irrotational [23, 26].

In spherical nuclei, the transition densities (TD) and transition currents (TC) for the transfer from the ground state $I^{\pi}\mu = 0^+0$ to the excited state ν with $1^- \mu$ read [54]

$$\delta\rho_{\nu\mu}(\mathbf{r}) = \langle \nu | \hat{\rho}(\mathbf{r}) | 0 \rangle = \delta\rho_{\nu}(r) Y_{1\mu}^*(\Omega) \quad (10)$$

$$\delta\mathbf{j}_{\nu\mu}(\mathbf{r}) = \langle \nu | \hat{\mathbf{j}}_{\text{c}}(\mathbf{r}) | 0 \rangle = i \sum_{L=0,2} j_{\nu}^{L\mu}(r) \mathbf{Y}_{1L\mu}^*(\Omega) \quad (11)$$

where $\hat{\rho}(\mathbf{r})$ is the density operator and $\hat{\mathbf{j}}_{\text{c}}(\mathbf{r}) = m/(e\hbar) \hat{\mathbf{j}}_{\text{c}}(\mathbf{r})$ is the scaled operator of the convection nuclear current, see definitions in the Appendix A. For simplicity, we use in TC plots only the convection current. The TD and irrotational TC are related by the continuity equation

$$-i \frac{m}{\hbar^2} E_{\nu} \delta\rho_{\nu\mu} = \nabla \cdot \delta\mathbf{j}_{\nu\mu}. \quad (12)$$

where

$$\nabla \cdot \delta\mathbf{j}_{\nu\mu} = i [\text{div } \delta j]_{\nu}(r) Y_{1\mu}^*(\Omega) \quad (13)$$

and

$$[\text{div } \delta j]_{\nu}(r) = \sqrt{\frac{1}{3}} \frac{d}{dr} j_{\nu}^{10}(r) - \sqrt{\frac{2}{3}} \left[\frac{d}{dr} + \frac{3}{r} \right] j_{\nu}^{12}(r). \quad (14)$$

The radial TD $\delta\rho_{\nu}(r)$ and divergence of TC $[\text{div } \delta j]_{\nu}(r)$ as well as angular-dependent TC (11) for $\mu = 0$ will be plotted and analyzed in Sec. 3 (in what follows we will omit the index μ). To suppress individual details of the states and highlight their general features, these variables are averaged over the dipole states in the chosen energy interval $[E_1, E_2]$ following the prescription [24, 26]. The averaging is done by summing the variables weighted by the dipole matrix elements $D_{\nu} = \langle \nu | \hat{M}_{10}^{\text{com}}(T=0) | 0 \rangle$. This amounts to

$$\delta\rho(r) = \sum_{\nu \in [E_1, E_2]} D_{\nu}^* \delta\rho_{\nu}(r), \quad (15a)$$

$$\delta\mathbf{j}(\mathbf{r}) = \sum_{\nu \in [E_1, E_2]} D_{\nu}^* \delta\mathbf{j}_{\nu 0}(\mathbf{r}), \quad (15b)$$

$$[\text{div } \delta j](r) = \sum_{\nu \in [E_1, E_2]} D_{\nu}^* [\text{div } \delta j]_{\nu}(r), \quad (15c)$$

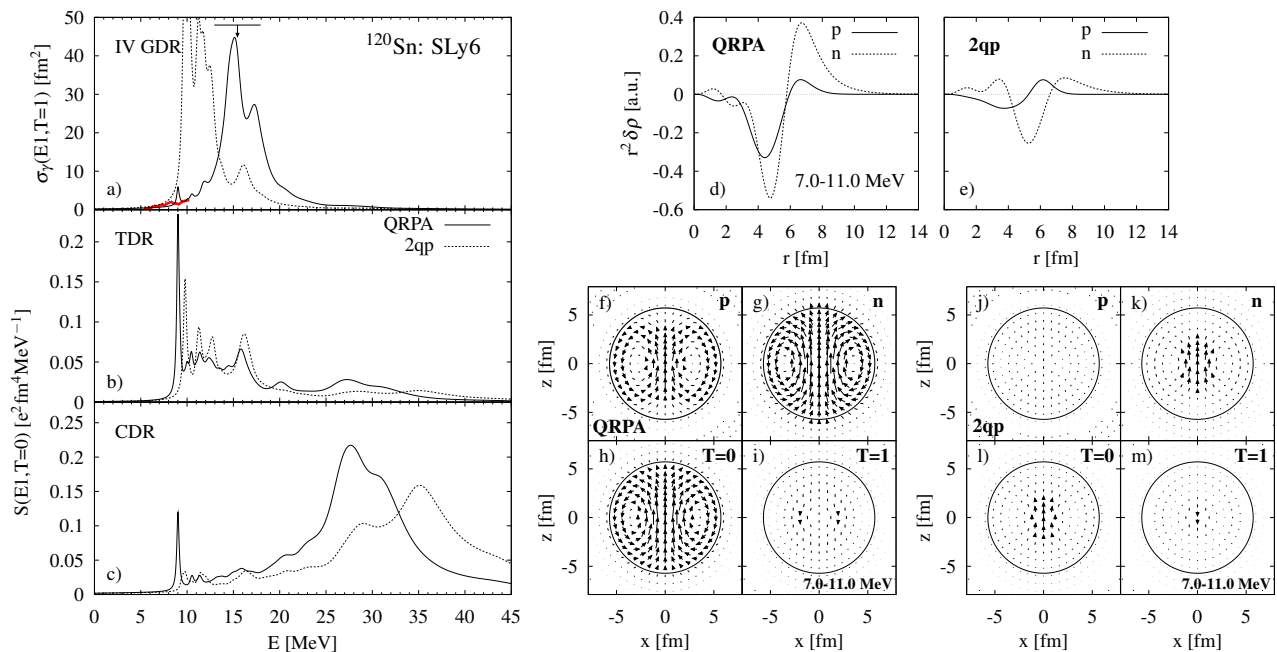


Fig. 2. (Color online) Results for ^{120}Sn computed with SLy6. Upper left block: IV dipole, IS toroidal, and IS compressional strength distributions. The experimental dipole strength at $E=5.5\text{--}10$ MeV [55] is marked by red open rhombuses. The experimental data [56] for IV GDR, maximum-strength energy and FWHM, are depicted by vertical arrow and horizontal line, respectively. Upper right block: TD integrated over the energy interval 7–11 MeV, left panel from QRPA and right panel from mere 2qp states. Lower right block: TC for proton, neutron, isoscalar ($T=0$), and isovector ($T=1$) flows; the flow pattern are shown for QRPA and mere 2qp states as indicated.

where $\delta\rho_\nu(r)$, $\delta\mathbf{j}_{\nu 0}(\mathbf{r})$ and $[\text{div } \delta\mathbf{j}]_\nu(r)$ are given by Eqs. (10), (11) and (14) using the sets of the effective charges corresponding to the proton, neutron, IS and IV transitions. The sets are listed in the Appendix A. The D_ν^* factors associate the proper weight to the contributions and render the expressions bilinear in $|\nu\rangle$ which, in turn, removes nonphysical dependence on the phase of $|\nu\rangle$, see [24, 26] for more detail. In the present study, the averaged TD and TC are calculated for both QRPA and 2qp states at the given energy interval.

In TD and TC from (10)-(11), the spurious admixtures arising due to the motion of the nuclear center-of-mass are eliminated following the prescription [31]. The unperturbed 2qp cases are corrected separately for protons and neutrons.

3 Results of the calculations

As a first example from our large selection of nuclei, we look at the case of ^{120}Sn computed with SLy6. This case is shown in Fig. 2. Its left part collects the strength functions for IV GDR, IS TDR and IS CDR (panels (a)-(c)). The compression strength is calculated with the current-dependent operator (8). In the right upper panels (d)-(e), we show the averaged proton and neutron radial TD $\delta\rho(r)$ from Eq. (15a). In the lower right panels (f)-(m), we demonstrate the averaged TC flow pattern from Eq. (15b). Both TD and TC are averaged over the PDR region 7-11

MeV. For each observable, the results from QRPA and unperturbed 2qp states are compared.

Following the panel (a), we will describe the experimental data [56] for the peak energy and FWHM of the IV GDR, which confirms the accuracy of our model. Further, panels (a)-(c) show that the PDR energy region coincides with the location of the low-energy parts of the toroidal and compressional strengths. This indicates that the nature of dipole states in this region is complicated. They should have both large vortical (TDR) and minor irrotational (probed by the compression dipole external field) fractions. In general, the IS TDR covers a large energy region 8-18 MeV. We will analyze only the low-energy part of the region, where both IS modes of our interest, TDR and PDR, coexist.

The residual interaction of QRPA downshifts the lowest toroidal and compressional peaks and considerably enhances their strength (and thus collectivity). At the same time, following our analysis, these dipole states still maintain rather large 2qp components (see Appendix B for more detailed information on the calculated dipole states in the PDR energy region and comparison of the obtained E1 strength with the experimental data [55]). The strong effect of the residual interaction is also seen in panels (d)-(e) for the radial TD: the neutron TD dominates at the nuclear surface for QRPA (which is often considered as justification of the a collective flow associated with a “pygmy resonance”) but not for 2qp case.

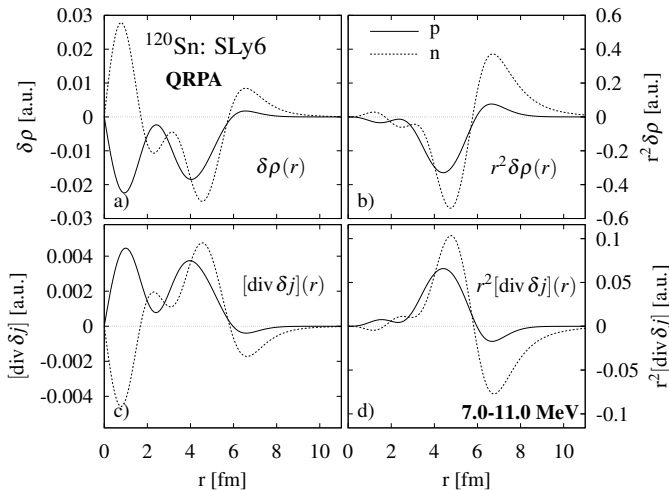


Fig. 3. Upper plots: averaged radial proton and neutron TD for QRPA (SLy6) states at the region 7–11 MeV in ^{120}Sn . Left and right panels exhibit TD without and with r^2 -weight. Bottom plots: the same but for the averaged radial part of the divergence of the nuclear current.

Complementing and more detailed information on the nuclear flow is provided by the angular-dependent TC shown in panels (f)-(m). In the 2qp case, neutron and $T=0$ pattern show weak signs of toroidal flow which then becomes very pronounced in QRPA. The dominant collective flow in the interval 7-11 MeV is obviously IS toroidal, see for comparison Fig. 1(b). The main contribution comes from neutrons in accordance with the dominance of neutron TD at the nuclear surface. We may state that the schematic picture of PDR as neutron oscillations against an $N = Z$ core is actually a crude map of the true mechanism behind, toroidal flow of neutrons at the nuclear boundary.

To gain a deeper insight into the relation between TDR and PDR, we present in Figs. 3-4 the calculated TD and TC in more detail. The main question is: can one explain the behavior of the neutron TD, in particular its maximum at the nuclear surface, by the neutron current which is basically toroidal?

In the upper panels of Fig. 3, we show the neutron and proton TD with and without r^2 -weight, which allows to discriminate the TD behavior at the nuclear surface and deep inside. We see that the neutron TD without r^2 -weight (panel (a)) exhibits three humps: positive at 0.5 – 2 fm, negative at 4 – 6 fm, and positive at 6 – 8 fm. In neutron TD with r^2 -weight (panel (b)), the first hump is much suppressed and the third hump at the surface is enhanced. Obviously, these three TD humps should be related to some essential structures in TC.

We know that TD and TC are linked by the continuity equation (CE) (12). The nuclear current enters the CE through its divergence. So only the *irrotational* fraction of TC contributes to CE while the dominant *vortical* toroidal current $\mathbf{j}_{\text{tor}} \sim \nabla \times (\nabla \times (r\mathbf{M}_{1\mu}^{\text{com}}(\mathbf{r})))$ [6, 8, 23] does not. The CE holds for each QRPA ν -state. However, the CE may be somewhat distorted for the *averaged* TD and TC (15)

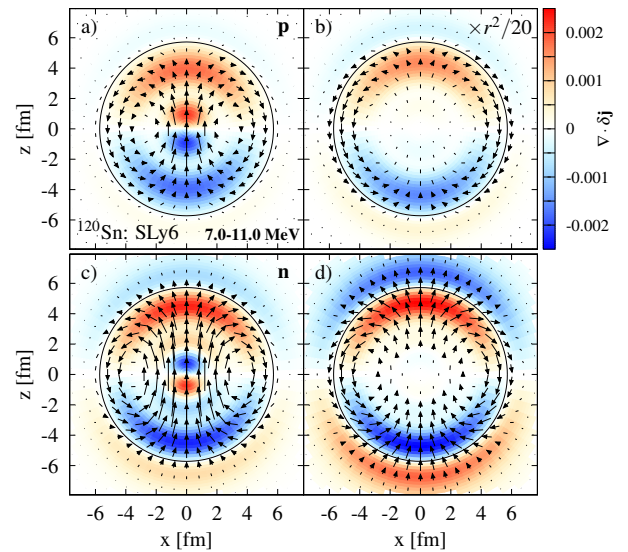


Fig. 4. (Color online) The averaged proton (upper panels) and neutron (bottom panels) TC and their angular-dependent divergences for QRPA (SLy6) states at the region 7–11 MeV. The variables are exhibited in $(x, y=0, z)$ -plane. Like in Fig. 2, the TC are depicted by arrows. The divergences are exhibited by color (tone) spots as indicated. Left and right panels show the variables without and with r^2 -weight. For a better view, the arrows for TC and color scaling with r^2 -weight in the right panels are decreased by the factor 1/20.

which are just the variables of our interest. To check this point, we exhibit in the lower panels of Fig. 3 the radial parts $[\text{div } \delta j](r)$ of the divergence of the averaged proton and neutron currents. We see that the behavior of the divergences strictly correlates with the behavior of the TD. So CE basically holds and the humps in the TD represent the inherent features of the actual (basically toroidal) TC.

Further, we show in Fig. 4 neutron and proton current distributions together with their angular-dependent divergences $[\text{div } \delta j](r)Y_{10}^*$. Since $Y_{10}^* \sim z/r$, the divergences in the upper ($z > 0$) and bottom ($z < 0$) parts of the plots differ only by their sign. So it is enough to inspect only the $z > 0$ parts of the plots.

Figure 4 shows a strong up-directed flux of protons and neutrons along z -axis. The flux definitely contains an irrotational flow and the main divergence spots are mainly located in its area. It is easy to see that, for both neutrons and protons, the divergence spots in Fig. 4 are in one-to-one correspondence with humps in the TD in Fig. 3. For neutrons, e.g., the divergence spot at $z \sim 1$ fm gives the positive TD hump at $0.5 < r < 1.5$ fm, the arc-like spot at $z \sim 4$ fm leads to the negative TD hump at $r = 4 - 6$ fm, and finally the arc-like spot at $z \sim 6$ fm results in the TD positive hump at $r = 6 - 8$ fm. The impact of the third outer-lying spot is strongly enhanced by r^2 -weight, see Fig. 3(d). Further, in accordance to TD, the proton and neutron divergences have a different sign at $z \sim 1$ fm and are in phase at $z \sim 4$ fm.

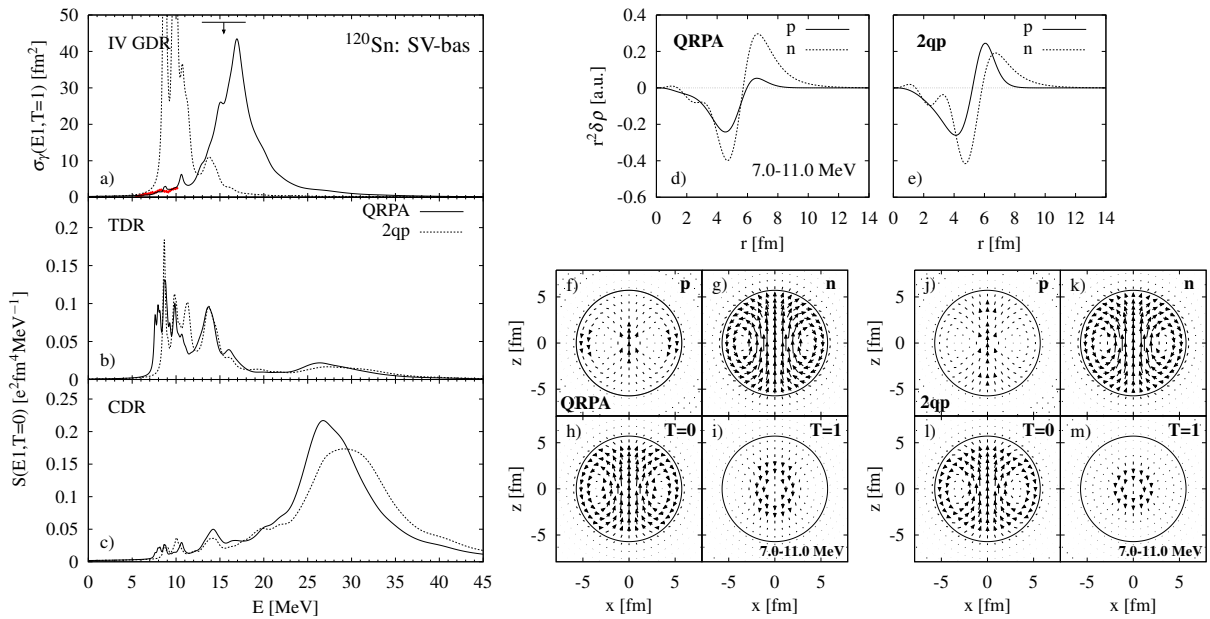


Fig. 5. (Color online) As in figure 2, but computed with SV-bas.

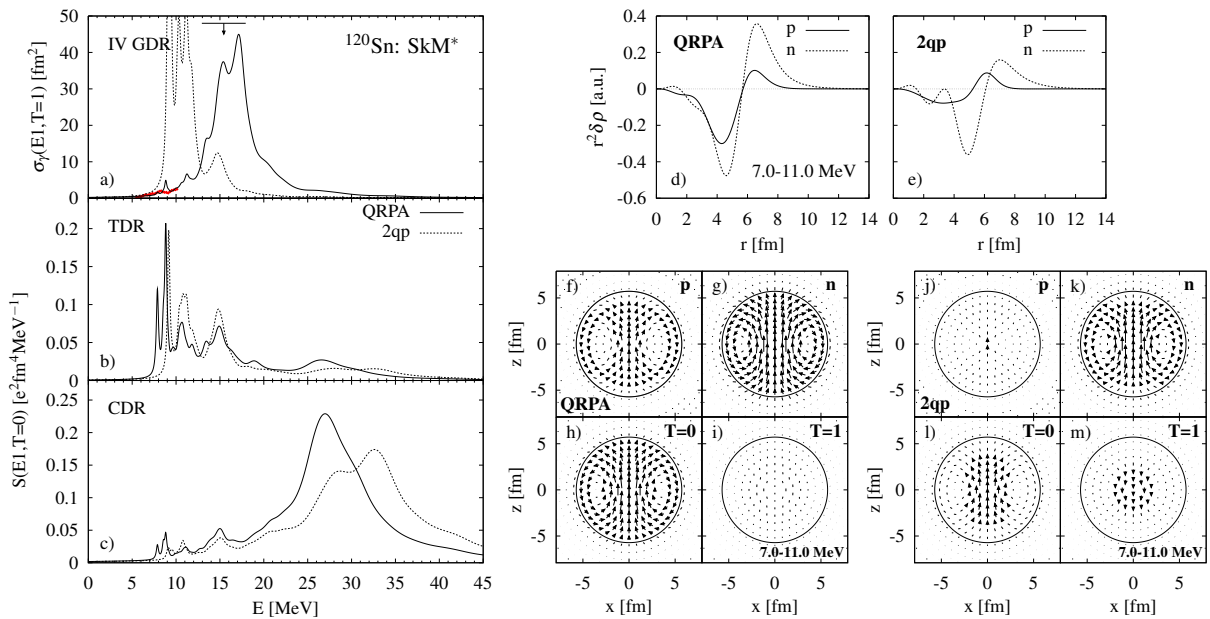


Fig. 6. (Color online) As in figure 2, but computed with SkM*.

Note that the first positive hump at 0.5 – 1.5 fm is a particular feature of ^{120}Sn (see for comparison TD in Figs. 7-14 for other nuclei). Instead, the next two humps, at 4–6 and 6–8 fm, persist in neutron TD for all considered nuclei.

The appearance of irrotational regions in predominantly toroidal flow can be explained by simple arguments. As mentioned above, the exact vortical toroidal current (Hill’s spherical vortex) $\mathbf{j}_{\text{tor}} \sim \nabla \times (\nabla \times (\mathbf{r} M_{1\mu}^{\text{com}}(\mathbf{r})))$ is a curl and so cannot produce the irrotational flow. However, as seen in Fig. 4, the actual toroidal motion is somewhat squeezed in x-direction. Indeed the curl centers at $|x| \sim 3 - 4$ fm

are rather ovals than circles. This squeezing leads to rectification of the flow in some regions (especially in the central up-flux) and thus to the appearance of the irrotational motion. This can also be treated as an admixture of a small irrotational compressional fraction [23]. As shown below, this effect takes place for all considered nuclei.

Finally, the correspondence between neutron TD and TC demonstrated in Figs. 3-4 allows to conclude that, in nuclei with a neutron excess, the hump in neutron TD at the nuclear surface (commonly treated as the proof of the PDR-like collective scheme) can be naturally produced by the basically toroidal current with some irrotational

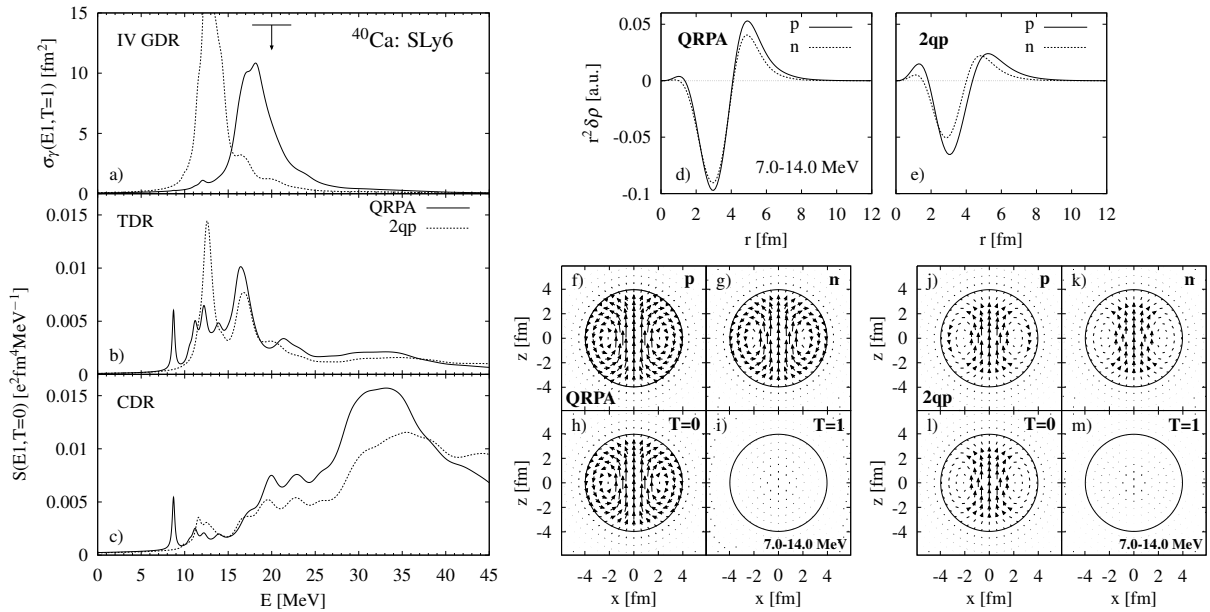


Fig. 7. (Color online) As in figure 2, but for ^{40}Ca . Experimental data [57] for IV GDR (peak energy and FWHM) are shown.

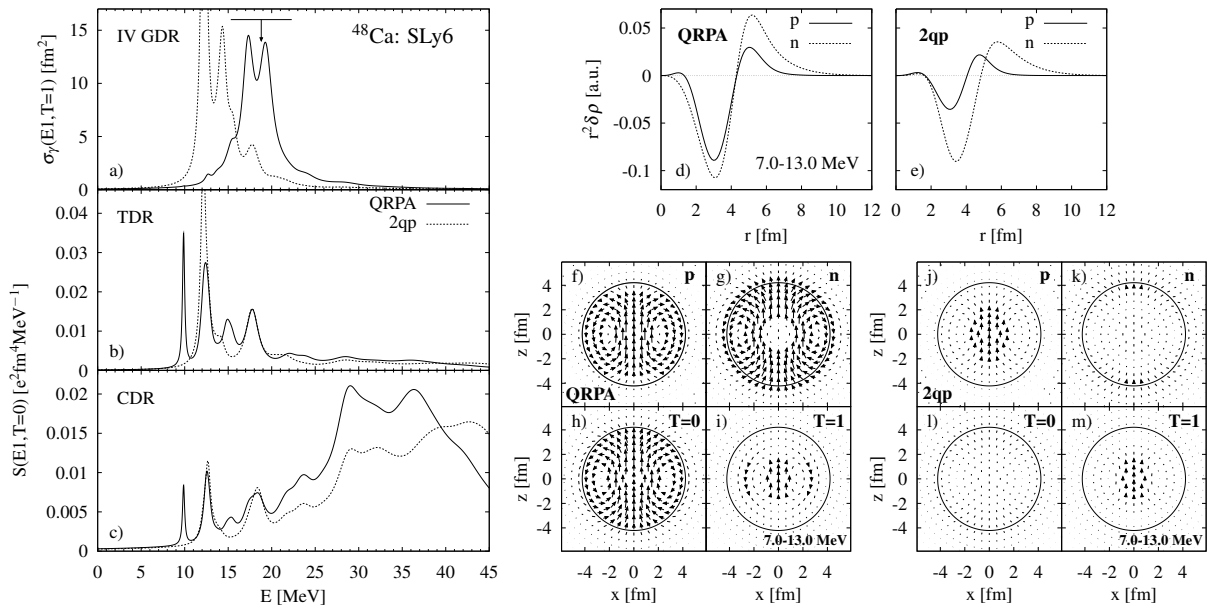


Fig. 8. As in figure 2, but for ^{48}Ca . Experimental data [58] for IV GDR (peak energy and FWHM) are shown.

fraction. The PDR scheme generally does not correspond to the actual TC and is only an oversimplified imitation of the true nuclear flow.

To check the sensitivity of our results to the choice of the Skyrme forces, we present in Figs. 5–6 the same variables as in Fig. 2, but now for the forces SV-bas and SkM*. Again we see that our calculations for IV GDR agree with the experimental data [56]. Almost all the conclusions drawn above for SLy6 for TDR/PDR come out the same way for SV-bas and SkM*. The visible difference is that the neutron TC for SV-bas and SkM* show a clear toroidal flow already in case of mere 2qp states

(see also comparison of SLy6, SV-bas and SkM* dipole states, given in Appendix B). This confirms our previous findings [25, 30] that the vortical toroidal flow is mainly of single-particle nature. The r^2 -weighted TD for SLy6, SV-bas and SkM* look somewhat different in the 2qp case but acquire the same persistent form in QRPA, characterized by a negative hump at 4–6 fm and a positive hump at 6–8 fm. As discussed above, this particular form is explained by the toroidal distribution of the nuclear flow in TC.

Since the performance of SLy6, SV-bas and SkM* is similar, we restrict ourselves in the following to results from SLy6 only. These results involve isotopic pairs $^{40,48}\text{Ca}$,

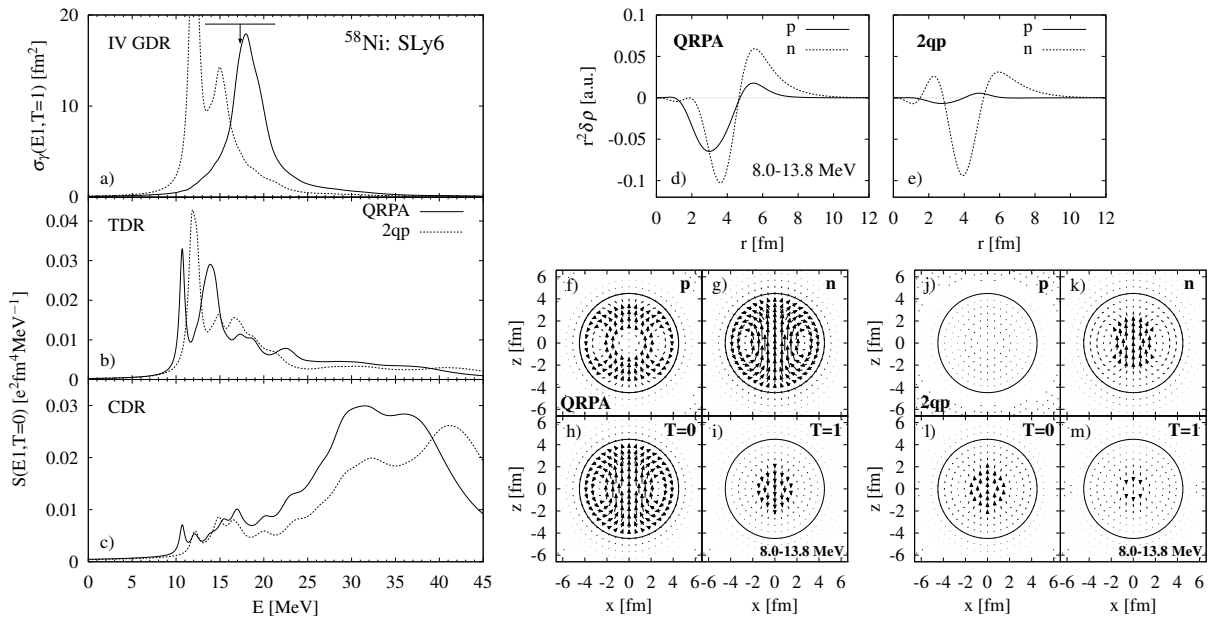


Fig. 9. As in figure 2, but for ^{58}Ni . Experimental data [59] for IV GDR (peak energy and FWHM) are shown.

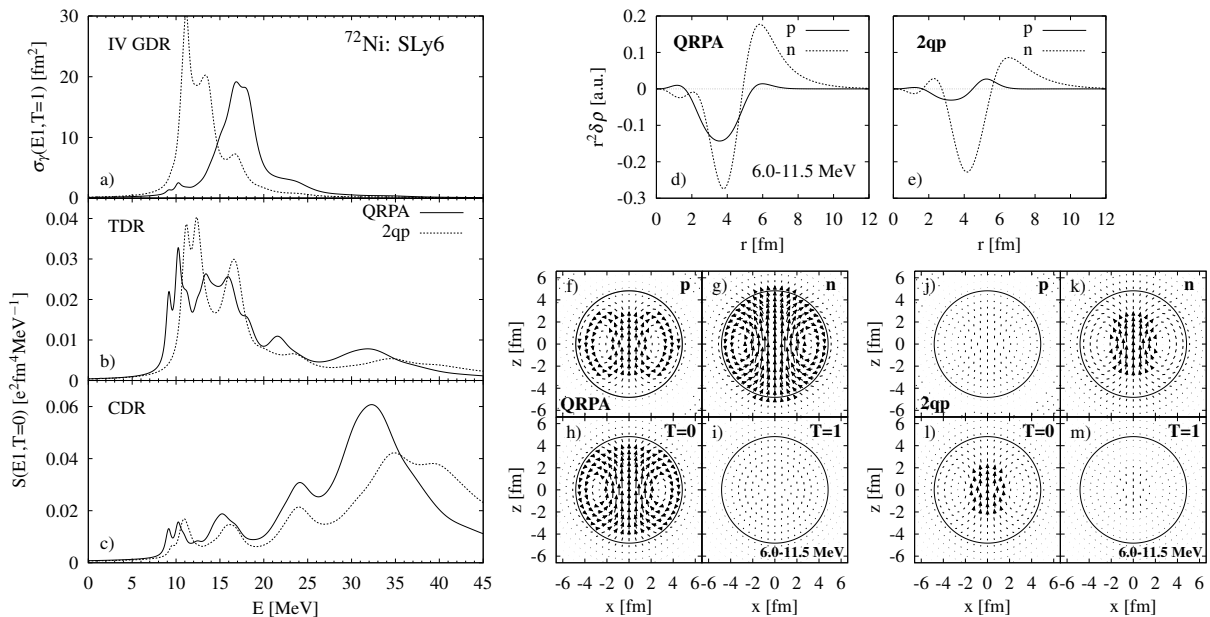


Fig. 10. As in figure 2, but for ^{72}Ni .

$^{58,72}\text{Ni}$, $^{90,100}\text{Zr}$, and $^{100,132}\text{Sn}$. Each pair includes one isotope without and one isotope with a large neutron excess.

Fig. 7 shows results for ^{40}Ca . This light nucleus with $N=Z$ should not exhibit PDR strength by definition. Indeed, we see from panels (d)-(e) that here the proton TD exceeds the neutron one at the nuclear surface in both 2qp and QRPA cases with the consequence that dipole strength in the PDR region is not visible.

At the same time, the TD from QRPA has the same particular form as in ^{120}Sn . As mentioned above, this form is explained just by the toroidal flow. Panel (b) shows that, at the energy region embracing the left wing of IV-GDR

(the typical PDR region), we have, indeed, rather large toroidal strength. The 2qp and QRPA TC in panels (f)-(m) also show toroidal flow. This flow is basically isoscalar with similar contributions of proton and neutrons (which is natural for $N=Z$ nucleus). So TDR does exist in ^{40}Ca where PDR strength is absent in principle.

Panel (b) shows that the enlarged TDR strength in ^{40}Ca covers a large energy region 8–20 MeV (embracing IV GDR). This strength is characterized by a few strong peaks. Our analysis shows that, unlike the lowest vortical IS TDR peak at 10 MeV, the higher peaks have a more complicated structure. They are formed by dipole

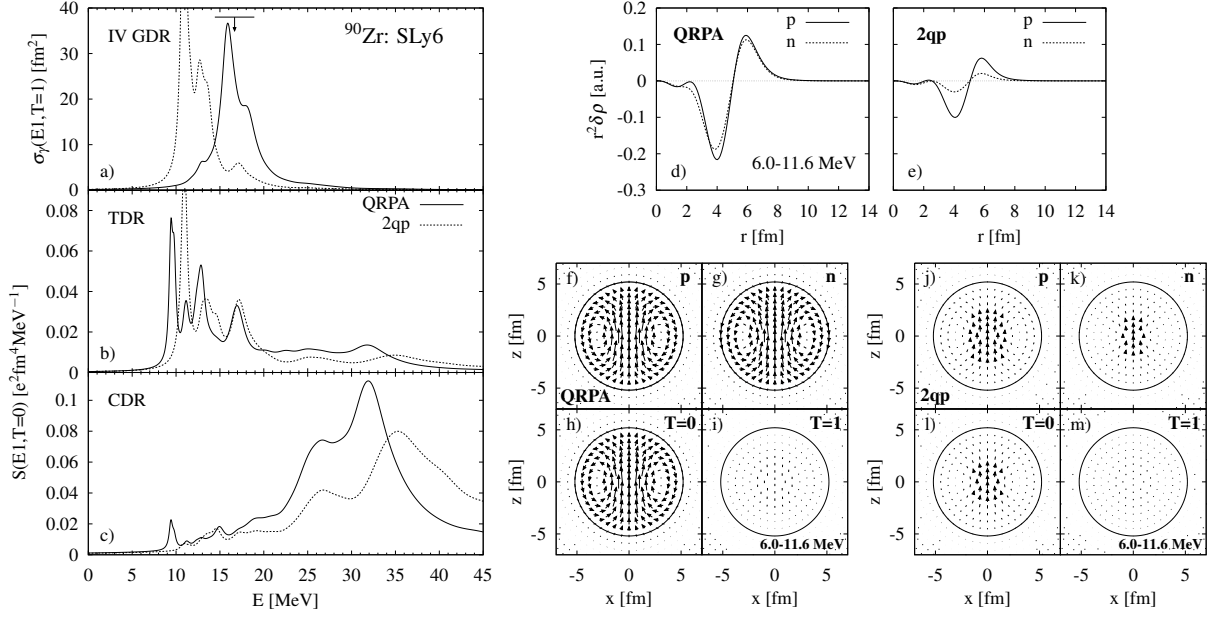


Fig. 11. As in figure 2, but for ^{90}Zr . Experimental data [60] for IV GDR (peak energy and FWHM) are shown.

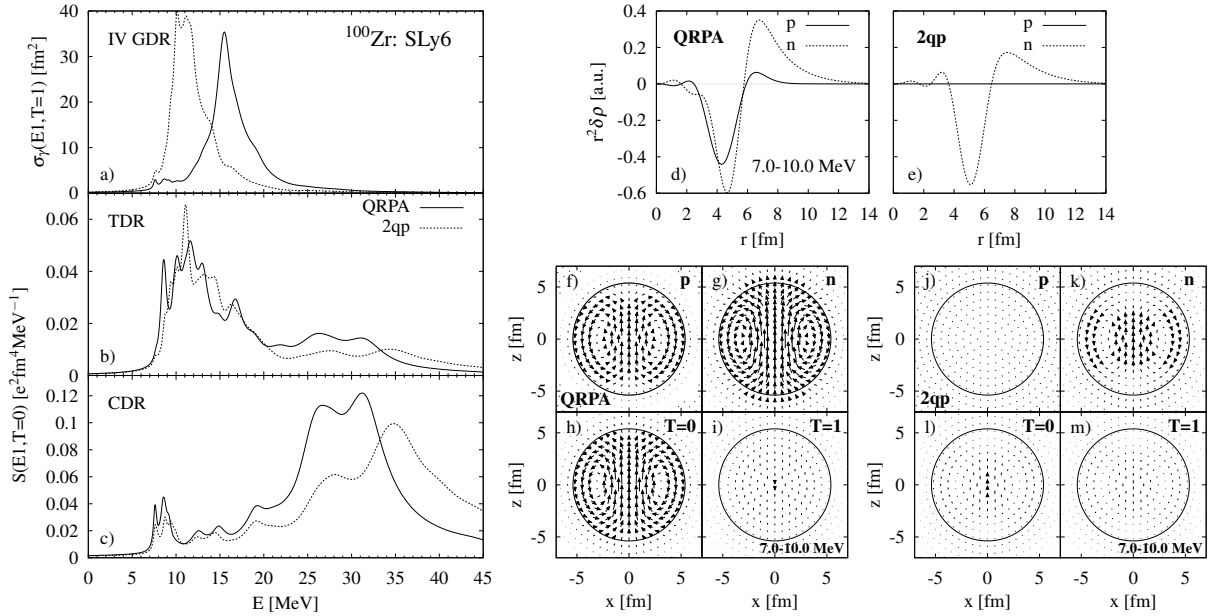


Fig. 12. As in figure 2, but for ^{100}Zr .

states with different collectivity and various ratios of vortical/irrotational and IS/IV components. The vorticity of these states arises from their major 2qp components. The vortical fractions contribute to the TDR strength while irrotational fractions produce E1 strength. The collectivity enhances both strengths. As seen below, this is a common feature of all the nuclei (with and without the neutron excess) considered in the present study. Finally note a good agreement of the calculated IV GDR with experimental data [57].

Fig. 8 shows the results for ^{48}Ca , a nucleus with significant neutron excess. The picture is basically the same as in

^{40}Ca . The only essential difference is the larger contribution of neutrons. This contribution enhances the toroidal strength at 7-11 MeV (panel (b)), renders the neutron TD dominant at the nuclear surface (panel (d)), and essentially enhances the IS toroidal current from QRPA as compared to the 2qp case. The latter is explained by an enhancement of the residual interaction due to the neutron excess. Note that we well describe the experimental data [58] for IV GDR.

The next results shown in Figs. 9-14 for the pairs $^{58,72}\text{Ni}$, $^{90,100}\text{Zr}$, and $^{100,132}\text{Sn}$ confirm (up to detail) all findings and conclusions drawn above from ^{120}Sn and $^{40,48}\text{Ca}$.

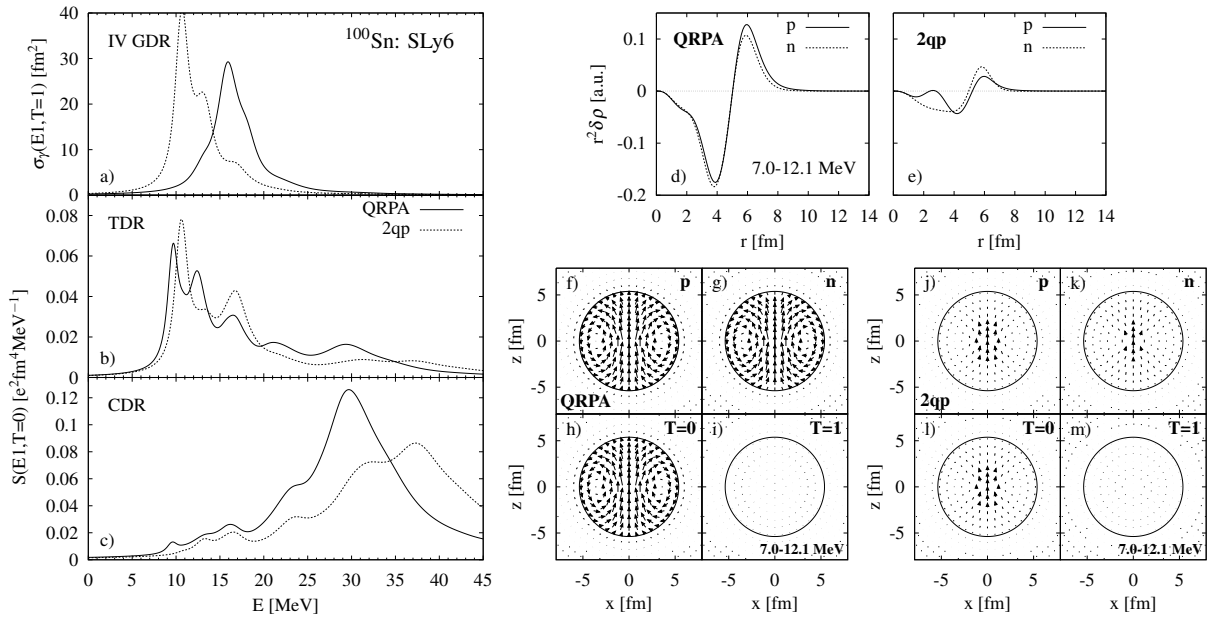


Fig. 13. As in figure 2, but for ^{100}Sn .

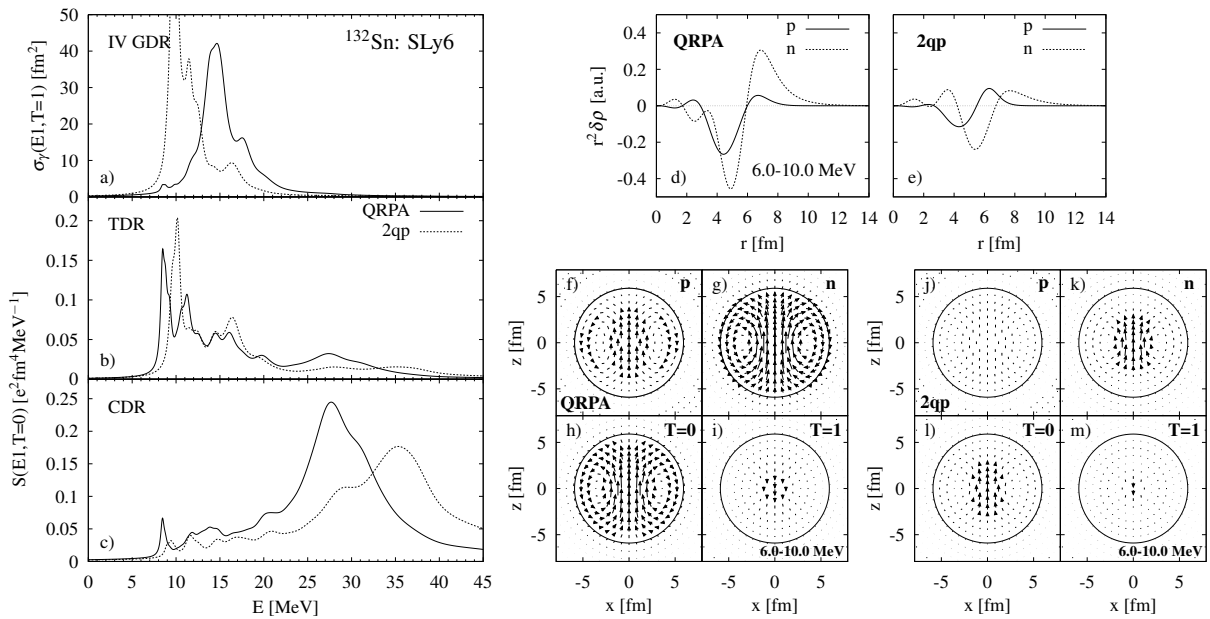


Fig. 14. As in figure 2, but for ^{132}Sn .

The results for IV GDR are in accordance with the experimental data for ^{58}Ni [59] and ^{90}Zr [60]. Finally, our systematics for four isotopic groups with $20 < Z < 50$, analyzed with three Skyrme forces, lead to the unambiguous conclusions that:

- Vortical TDR is a general feature of nuclear dipole excitations. It forms a broad structure concentrated at 7-20 MeV. Its low-energy IS part sharing the same energy with PDR is the main subject of our study.
- The toroidal character of the flow is explicitly confirmed by the TC.

- The toroidal flow is somewhat squeezed, which results in appearance of local irrotational regions. These regions contribute to the TD and produce an irrotational (e.g. compressional) response,
- TD and toroidal TC have one-to-one correspondence.
- In nuclei with a large neutron excess, the actual flow at the nuclear surface can be roughly imitated by the picture of an oscillating neutron surface often associated with a PDR.

The persistence of the TDR in various nuclei can be explained by simple arguments. As seen from the panels

(a) of Figs. 2 and 5-14, we have a bunch of unperturbed 2qp dipole strength in each nucleus (dashed line). This dipole strength is produced by $E1(\Delta\mathcal{N} = 1)$ transitions between the neighbor shells, where \mathcal{N} is the principle shell quantum number. The energy of the bunch is typically $E_{\text{sp}} \approx 41A^{-1/3}$ [21]. This 2qp strength has both irrotational and vortical fractions. The IV dipole residual interaction (corresponding basically to Tassie mode $rY_{1\mu}$) is strongly repulsive and up-shifts the irrotational strength to form the large IV GDR but does not affect IS strength, especially its vortical (non-Tassie) fraction. A large part of the vortical strength remains at E_{sp} and becomes even dominant there, thus forming the TDR.

Most of the Figs. 2 and 5-14 show a significant enhancement of the toroidal flow by the QRPA residual interaction. This takes place in all considered nuclei, except perhaps for ^{40}Ca and ^{120}Sn (SV-bas). Thus we see that, although the toroidal flow is basically of 2qp origin [23, 25, 30, 43, 54], it is considerably enhanced by the residual interaction which renders the toroidal flow more collective.

Note that the profile of the calculated TD corresponds to toroidal flow rather than to PDR-like pattern. The main difference lies in the TD at the nuclear interior. Following the PDR picture, the nuclear core with $N=Z$ should move as a whole piece against the cloud of the excess neutrons at the surface. This should give a basically vanishing TD in the whole nuclear interior. However, for all isotopes considered in our study, the calculated TD exhibit in the interior a sequence of positive and negative humps. As discussed above, such behavior is typical for dominantly 2qp states. It stays in accordance with the toroidal distribution of the TC, but contradicts a collective PDR picture.

4 Discussion

For better understanding of the relation between PDR and TDR, it is instructive to compare their main features.

a) The principle difference between TDR and PDR is that TDR is mainly vortical while PDR is irrotational, i.e. their velocities fulfill the relations $\nabla \cdot \mathbf{v}_{\text{TDR}} \approx \mathbf{0}$, $\nabla \times \mathbf{v}_{\text{PDR}} = \mathbf{0}$. The vortical TDR, unlike the PDR, does not contribute to the continuity equation and Thomas-Reiche-Kuhn sum rule.

b) TDR is determined by the convective transition current $\delta\mathbf{j}_c$ while PDR by the transition density $\delta\rho$. The magnetization part of the nuclear current can significantly conceal the manifestation of the convective toroidal excitations in (e, e') and other reactions [61].

c) TDR exists in all the nuclei (with exception of the smallest ones) independently on whether they have or have not neutron excess (see arguments at the end of the previous section). Instead, PDR can exist only in nuclei with a noticeable neutron excess.

d) A genuine PDR assumes a collective flow of the neutron excess. Instead, TDR has the mean field origin and combines both unperturbed (2qp) and collective flows.

e) As shown above, the actual PDR strength can be treated as a minor irrotational fraction of squeezed toroidal dipole states. If so, then PDR fraction can be used as a

doorway state for generation of the toroidal flow in reactions where vortical excitations are not directly produced.

f) TDR and PDR represent two concepts of dipole motion with a fixed center of mass. In both modes, the central flow coexists with the opposite peripheral flow.

g) TDR is a broad structure mainly located at 7–20 MeV. Its low-energy IS part lies at the PDR energy region. PDR and TDR are formed from the residues of dipole strength, remaining after the upshift of the main irrotational dipole strength to the IV giant dipole resonance.

h) Both PDR and TDR have IS and IV components and are, to large extent, isospin mixed [23, 41, 42]. In both resonances, IS strength lies lower than IV one. In the present study, we compare only low-energy IS PDR and TDR parts. Their IV parts need an independent and, perhaps, more complicated analysis. For example, as compared to IS TDR, the IV TDR is more affected by the magnetization current [23].

Dipole strength in the PDR region is important in many aspects. It is sensitive to the nuclear neutron skin and so may help to confine the nuclear symmetry energy and the isospin-dependent part of the nuclear equation of state, see e.g. reviews [2, 42]. Besides, this resonance is located near the neutron separation threshold S_n and so can have strong impact on the astrophysical r-process [62]. A great number of calculations has been already performed for dipole strength in the PDR region. We have worked out here the mainly toroidal nature of these low-energy dipole states, which raises the question whether one would need to revise all these calculations. This is not necessary if the calculations employ the fully detailed 2qp structure of the dipole states (e.g. within QRPA approaches) which takes properly into account the balance between major toroidal and minor irrotational contributions. In the IV dipole strength, relevant for photo-absorption, only the minor irrotational fraction is visible while the toroidal contribution is negligible. In other reactions (e.g. inelastic electron scattering at large angles), the effect of the vortical toroidal contribution can be essential [61, 63, 11]. It is thus worthwhile to inspect the ability of various reactions to identify the vortical toroidal mode as we will do in the next paragraphs.

The IS TDR constitutes the low-energy part of IS GDR observed in various isoscalar reactions, first of all in (α, α') (see e.g. [13, 14, 15, 16, 17, 18, 19] and reviews [2, 41, 42]). However, our recent Skyrme QRPA calculations show that this treatment can be disputed [22]. Most probably, the observed low-energy hump in IS GDR is not a merely TDR structure but a mixture of of toroidal and compressional fractions. Moreover, the dipole response in (α, α') reaction is mainly determined by the transition density while the toroidal mode is generated by the vortical current which is not confined by the continuity equation. So, the (α, α') reaction is perhaps not suited to search the IS TDR and the direct observation of the toroidal mode remains an open problem.

An alternative would be to search TDR strength in reactions like $(^{17}\text{O}, ^{17}\text{O}')$, (d, d') , high-resolution (p, p') under extreme forward angles, nuclear fluorescence, etc (see

the recent review [42] and references therein). Both polarized and unpolarized projectiles could be used since the vortical flow, in principle, could cause a polarization of emerging products. The reactions combining inelastic scattering with γ -decay, $(\alpha, \alpha'\gamma)$, $(^{17}\text{O}, ^{17}\text{O}'\gamma)$ and $(p, p'\gamma)$, can be also probed. A general problem is that we still do not know definite fingerprints of the vortical flow in these reactions. The relevant predictions need yet to be developed within modern theoretical methods embracing both nuclear structure and reaction mechanisms.

Among promising reactions for search TDR, one should also mention inelastic electron scattering (e, e') [61, 63, 64, 65] or more detailed versions like $(e, e'\gamma)$ [66, 67] and scattering of polarized electrons [68]. The TDR form factor is transversal and can significantly contribute to the scattering of electrons at large angles. However, we meet here a strong competition with the contribution of the magnetization nuclear current [61]. As a result, we usually have a mixture of the convective (TDR) and magnetization vortical contributions. Hopefully, the convective TDR form factor can be extracted from experimental (e, e') data using a decomposition prescription [61]. The reaction $(e, e'\gamma)$ also looks encouraging since the angle of the outgoing photon can be sensitive to the vorticity of the excited state. However, in reactions with electrons, we also do not know yet possible fingerprints of the TDR.

In general, it seems that theory and experiment thus far were not able to propose robust signals for an unambiguous identification of intrinsic vortical electric dipole modes. This remains still a challenge.

In this connection, the exploration of individual vortical toroidal 1^- states in light nuclei looks promising. Such states were predicted in ^{10}Be , ^{12}C , ^{16}O , ^{20}Ne and ^{24}Mg [29, 30, 35, 36, 37, 38, 39]. They can be much easier identified than TDR in heavier nuclei. For example, in ^{24}Mg , the individual toroidal state should be the lowest $I^\pi K = 1^-1$ excitation near the α -particle threshold [29].

5 Conclusions

In this paper, we analyzed from a theoretical perspective the structure of dipole modes in the low-energy range of 6–13 MeV. The survey was based on the quasiparticle random-phase approximation (QRPA) built fully self-consistently on top of a Skyrme HF+BCS description of the nuclear ground state [22, 34, 46, 48]. A large selection of nuclei (Ca, Ni, Zr, Sn) was considered and three different Skyrme parametrizations were used to probe the generality of the findings. For each element, we consider at least two isotopes, one with low (or zero) neutron excess and another one with large neutron excess in order to probe the impact of excess neutrons predominantly gathering at the nuclear surface. Particular attention was paid to the relation between the isoscalar (IS) toroidal dipole resonances (TDR) and the low-energy dipole states, often denoted as the IS part of the pygmy dipole resonance (PDR). We investigate the structure of the modes in terms of dipole strength function, transition density (TD), and transition

current densities (TC) visualized as a flow pattern. As further analyzing tool, we compare the QRPA states with the uncoupled mere two-quasiparticle (2qp) states which are the BCS generalization of the one-particle-one-hole states in Hartree-Fock. The main piece of analysis is done for the spherical nucleus ^{120}Sn .

In all the nuclei, independently of the neutron to proton ratio, we have found a broad distribution of IS toroidal strength. The concentration of this strength at 6–20 MeV is denoted as the toroidal dipole resonance (TDR). In our study, we address the low-energy part of the IS TDR located at 6–13 MeV, i.e. at the same energy region as the PDR. The persistence of the TDR is explained in terms of shell structure. The dominant pure 2qp dipole states come from transitions over one major shell and cover exactly the considered energy range 6–13 MeV. The strong isovector (IV) residual interaction in QRPA shifts the major fraction of (irrotational) IV dipole strength far up into the region of the isovector giant dipole resonance (IV GDR) while the IS vortical states remain much less affected by QRPA and stay in their original energy range. The IV GDR is thus characterized by irrotational flow while the dominantly vortical flow remains in the low energy region. Dipole states with energy above IV GDR can also exhibit vorticity due to their large 2qp components.

Nuclei with large neutron excess also show some peaks with considerable IV dipole strength in the PDR region and this comes along with considerable mixing of IS and IV strength [40, 43]. However, this IV branch of PDR and its isospin mixing was not scrutinized here and remains an issue for a subsequent survey. The same holds for the impact of complex configurations beyond mere 2qp states which may be non-ignorable [12, 20, 40] and should be checked.

In all considered nuclei, the flow pattern (from CD) at 6–13 MeV is obviously toroidal. The toroidal motion is somewhat squeezed, which creates, in addition to the dominant vortical flow, the local irrotational regions contributing to the TD. In the nuclei with neutron excess, the TD has a neutron hump at the nuclear surface, which is usually considered as the main justification of a collective picture for the PDR. What we find is that this hump and other features of TD can be explained by the toroidal TC.

Altogether, our systematic investigation leads to the unambiguous conclusion that IS PDR strength is actually an outflow of the underlying toroidal mode in nuclei with the neutron excess. The collective pygmy-like picture of an oscillating neutron surface is only a rough imitation of the actual nuclear flow. Even after the energy averaging, the calculated TD exhibit large fluctuations deep into the inside of the nucleus, which is characteristic of single-particle structure. Toroidal flow is seen already in 2qp current distributions, i.e. has basically mean-field origin. The QRPA residual interaction enforces toroidal flow and introduces some collectivity.

We briefly discussed various reactions, first of all (α, α') and (e, e') , which could be used to search and identify vortical toroidal modes. It is known that in (e, e') reactions the impact of the vortical flow can be essential if not dominant [30, 61, 63]. Unfortunately, theory and exper-

iment have no yet come to robust proposals for unambiguous identification of intrinsic vortical electric modes. Such proposals should take into account both nuclear structure and reaction mechanisms and thus may be involved. This remains a challenge and concentration on exploration of TDR will probably be the most promising starting point.

The work was partly supported by Votruba-Blokhincev (Czech Republic-BLTP JINR) and Heisenberg-Landau (Germany - BLTP JINR) grants. A.R. is grateful for support from Slovak Research and Development Agency under Contract No. APVV-15-0225, and Scientific Grant Agency VEGA under Contract No. 2/0129/17. J.K. acknowledges the grant of Czech Science Agency (Project No. 19-14048S).

A Nuclear density and current operators

The density operator reads [23]

$$\hat{\rho}(\mathbf{r}) = \sum_{q=n,p} e_{\text{eff}}^q \sum_{k \in q} \delta(\mathbf{r} - \mathbf{r}_k) \quad (\text{A.1})$$

where e_{eff}^q are proton and neutron effective charges.

The operator of the full nuclear current consists of the convective and magnetic (spin) parts [23]

$$\hat{\mathbf{j}}_{\text{nuc}}(\mathbf{r}) = \hat{\mathbf{j}}_{\text{c}}(\mathbf{r}) + \hat{\mathbf{j}}_{\text{m}}(\mathbf{r}) = \frac{e\hbar}{m} \sum_{q=n,p} (\hat{\mathbf{j}}_{\text{c}}^q(\mathbf{r}) + \hat{\mathbf{j}}_{\text{m}}^q(\mathbf{r})) \quad (\text{A.2})$$

where

$$\hat{\mathbf{j}}_{\text{c}}^q(\mathbf{r}) = -i \frac{e_{\text{eff}}^q}{2} \sum_{k \in q} (\delta(\mathbf{r} - \mathbf{r}_k) \nabla_k + \nabla_k \delta(\mathbf{r} - \mathbf{r}_k)) \quad (\text{A.3})$$

$$\hat{\mathbf{j}}_{\text{m}}^q(\mathbf{r}) = \frac{g_s^q}{2} \sum_{k \in q} \nabla \times \hat{\mathbf{s}}_{qk} \delta(\mathbf{r} - \mathbf{r}_k), \quad (\text{A.4})$$

and $\hat{\mathbf{s}}_q$ is the spin operator, μ_N is the nuclear magneton, g_s^q is the spin g-factor, k numerates the nucleons. The isoscalar strength functions (2) are calculated with the effective charges $e_{\text{eff}}^p = e_{\text{eff}}^n = 0.5$ and g-factors $g_s^p = g_s^n = 0.5\eta(\bar{g}_s^p + \bar{g}_s^n)$. Here $\bar{g}_s^p = 5.58$ and $\bar{g}_s^n = -3.82$ are the bare g-factors and $\eta = 0.7$ is the quenching parameter [21].

For TD and TC, we consider four options of the density and current operators (proton, neutron, isoscalar ($T=0$), isovector ($T=1$)), fixed in (15) by the index $\beta = p, n, 0$, and 1. In TC we use only the convection current.

Finally, four options are fully determined by the effective charges:

$$\beta = p : e_{\text{eff}}^p = 1, e_{\text{eff}}^n = 0, \quad (\text{A.5})$$

$$\beta = n : e_{\text{eff}}^p = 0, e_{\text{eff}}^n = 1, \quad (\text{A.6})$$

$$\beta = 0 : e_{\text{eff}}^p = e_{\text{eff}}^n = 0.5, \quad (\text{A.7})$$

$$\beta = 1 : e_{\text{eff}}^p = \frac{N}{A}, e_{\text{eff}}^n = -\frac{Z}{A}. \quad (\text{A.8})$$

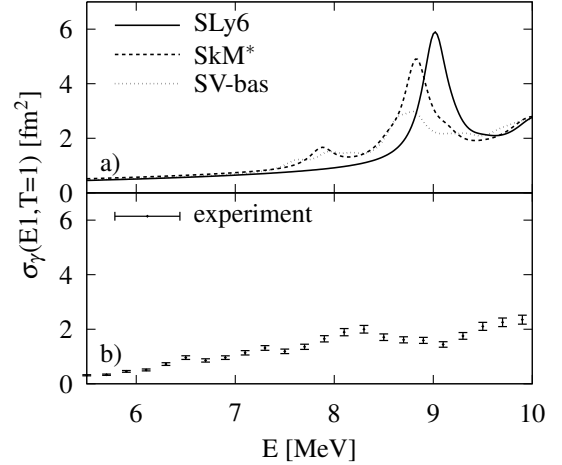


Fig. 15. The photoabsorption in ^{120}Sn at energy 5.5 - 10 MeV: (a) calculated within QRPA with the Skyrme forces SLy6, SV-bas and SkM*; (b) extracted from (p, p') data [55].

B Low-energy dipole states in ^{120}Sn

To demonstrate the accuracy of our numerical results, it is worth to compare the calculated photoabsorption in ^{120}Sn with recent experimental data obtained in inelastic proton scattering under extreme small angles [55]. This reaction allows to get the dipole strength below and above the neutron threshold energy S_n within one experiment. Under almost zero scattering angles, the reaction is dominated by the Coulomb excitation [69].

In Fig. 15, the photoabsorption calculated with SLy6, SV-bas and SkM* is compared with the photoabsorption extracted from (p, p') data [55]. All three Skyrme forces give a significant peak at 8.2-9.5 MeV which corresponds to the experimentally observed resonance-like structure at 8.3 MeV. The experimental EWSR strength up to 9 MeV is 2.3(2)%. Our calculations give for the interval 5.5 - 10 MeV the values 1.3% (SLy6) and 1.1% (SV-bas, SkM*).

In Table I, the features of the calculated dipole states lying below 9.2 MeV are presented. It is seen that for SLy6 dipole states appear only above 9 MeV. Instead, SV-bas and SkM* dipole spectra start at 7.5 - 8 MeV and embrace more levels. The difference can be explained by the effective mass which is much smaller for SLy6 (0.7) than for SV-bas (0.9) and SkM* (0.8). For all three Skyrme forces, the states are rather collective: contributions of the largest 2qp components do not exceed 60% of the state norm (with exception of 7.87-MeV state in SkM*). This explains the significant effect of the residual QRPA interaction shown in Sec. 3. Distributions of E1 strength are different. In SLy6 and SkM*, $B(E1)_\nu$ values are peaked at 9.01-MeV and 8.83-MeV states, thus producing the humps visible in Fig. 15 (a). Instead, in SV-bas the strength is spread more uniformly. In general, for SV-bas and SkM*, dipole strengths are more distributed and less collective than for SLy6. This explains why for SV-bas and SkM*

Table 1. The lowest dipole states with $E < 9.2$ MeV in ^{120}Sn , calculated with Skyrme forces SLy6, SV-bas and SkM*. For each state, energies E_ν , $B(E1)_\nu$ values for $0^+0_{\text{gr}} \rightarrow 1^-_0$ transitions and maximal 2qp components (with their contributions to the state norm) are shown.

Force	E_ν MeV	$B(E1)_\nu$ $e^2\text{fm}^2$	main 2qp component	
SLy6	9.01	0.199	nn	$[3p_{3/2} 3s_{1/2}]$ 21%
	9.19	0.015	nn	$[3p_{3/2} 2d_{3/2}]$ 52%
SV-bas	7.61	0.017	nn	$[2f_{7/2} 1g_{7/2}]$ 39%
	7.94	0.024	pp	$[2p_{1/2} 3s_{1/2}]$ 34%
	8.17	0.013	nn	$[3p_{3/2} 2d_{3/2}]$ 27%
	8.63	0.052	nn	$[2f_{7/2} 1g_{7/2}]$ 26%
	8.82	0.055	nn	$[3p_{3/2} 2d_{3/2}]$ 36%
	8.99	0.007	nn	$[3p_{3/2} 3s_{1/2}]$ 22%
	9.15	0.014	nn	$[3p_{3/2} 2d_{3/2}]$ 47%
SkM*	7.87	0.035	nn	$[2f_{7/2} 1g_{7/2}]$ 75%
	8.55	0.018	nn	$[3p_{3/2} 2d_{3/2}]$ 57%
	8.83	0.157	nn	$[2f_{7/2} 1g_{7/2}]$ 22%
	9.13	0.020	nn	$[3p_{3/2} 2d_{3/2}]$ 33%
	9.18	0.001	nn	$[3p_{1/2} 3s_{1/2}]$ 39%

the toroidal mode is pronounced in TC already in 2qp case.

Though our QRPA calculations roughly reproduce the structure observed at 8.3 MeV [55], they overestimate its energy. Besides, in contrast to the experiment, the calculations do not give dipole states below 7 MeV. These discrepancies can be partly explained by the fact that we do not take into account the coupling with complex configurations (CCC). Following theoretical estimations in [55], CCC can be important for the actual distribution of the dipole strength. At the same time, even models with CCC still provide quite different dipole distributions [55].

Table I shows that dipole states in the PDR region significantly vary in collectivity and structure and so can result in different transition densities (TD) and transition currents (TC). To overcome this trouble, TD and TC shown in Sec. 3 are averaged by a special way described in Ref. [24]. This allows to suppress individual details of the states and highlight their common general features. Moreover, this partly simulates the smearing CCC effect.

C Acronyms

Below we list the acronyms used throughout this paper:

QRPA	quasi-particle random-phase-approximation
GDR	giant dipole resonance
TDR	toroidal dipole resonance
CDR	compressional dipole resonance
PDR	pygmy dipole resonance (region)
TD	transition density
TC	transition current
IS	isoscalar ($T = 0$)
IV	isovector ($T = 1$)
E1	electric dipole
CE	continuity equation

References

1. S. F. Semenko, Sov. J. Nucl. Phys. **34**, 356 (1981).
2. N. Paar, D. Vretenar, E. Kyan, G. Colo, Rep. Prog. Phys. **70**, 691 (2007).
3. V.O. Nesterenko, J. Kvasil, A. Repko, W. Kleinig, and P.-G. Reinhard, Phys. Atom. Nucl. **79**, 842 (2016).
4. M. J. M. Hill, Phil. Trans. Roy. Soc. London A **185**, 213 (1894).
5. L. M. Mime-Thomson, *Theoretical hydrodynamics*, 4th ed., ch. 18 (Macmillan, New York, 1960).
6. S. I. Bastrukov, Ş. Mişicu, and A. V. Sushkov, Nucl. Phys. A **562**, 191 (1993).
7. E.B.Balbutsev, I.V.Molodtsova, and A.V.Unzhakova, Europhys. Lett. **26**, 499 (1994).
8. Ş. Mişicu, Phys. Rev. C **73**, 024301 (2006).
9. G. Colo, N. Van Giai, P.F. Bortignon, and M. R. Quaglia, Phys. Lett. **B485**, 362 (2000).
10. D. Vretenar, N. Paar, P. Ring, and T. Nikšić, Phys. Rev. C **65**, 021301(R) (2002).
11. A. Richter, Nucl. Phys. A **731**, 59 (2004).
12. P. Papakonstantinou, V.Yu. Ponomarev, R. Roth, and J. Wambach, Eur. Phys. J. A **47**, 14 (2011).
13. H. P. Morsch, M. Rogge, P. Turek, and C. Mayer-Borick, Phys. Rev. Lett. **45**, 337 (1980).
14. G. S. Adams, K. van der Borg, T. Ishimatsu, H. P. Morsch, A. van der Woude, and F. E. Bertrand, Phys. Rev. C **33**, 2054 (1986).
15. B. F. Davis et al., Phys. Rev. Lett. **79**, 609 (1997).
16. H. L. Clark, Y. W. Lui, and D. H. Youngblood, Phys. Rev. C **63**, 031301(R) (2001).
17. D. H. Youngblood, K. van der Borg, T. Ishimatsu, H. P. Morsch, A. van der Woude, and F. E. Bertrand, Phys. Rev. C **69**, 054312 (2004).
18. M. Uchida et al., Phys. Lett. B **557**, 12 (2003).
19. M. Uchida et al., Phys. Rev. C **69**, 051301(R) (2004).
20. N. Ryezayeva et al., Phys. Rev. Lett. **89**, 272502 (2002).
21. M. N. Harakeh and A. van der Woude, *Giant Resonances* (Clarendon Press, Oxford, 2001).
22. A. Repko, J. Kvasil, V.O. Nesterenko, and P.-G. Reinhard, Eur. Phys. J. A **53**, 221 (2017).
23. J. Kvasil, V.O. Nesterenko, W. Kleinig, P.G. Reinhard, and P. Vesely, Phys. Rev. C **84**, 034303 (2011).
24. A. Repko, P.-G. Reinhard, V.O. Nesterenko, and J. Kvasil, Phys. Rev. C **87**, 024305 (2013).
25. V.O. Nesterenko, A. Repko, P.-G. Reinhard, and J. Kvasil, EPJ Web of Conf., **93**, 01020 (2015).
26. P.-G. Reinhard, V.O. Nesterenko, A. Repko, and J. Kvasil, Phys. Rev. C **89**, 024321 (2014).
27. J. Kvasil, V.O. Nesterenko, W. Kleinig, D. Bozik, P.-G. Reinhard, and N. Lo Iudice, Eur. Phys. J. A, **49**, 119 (2013).
28. J. Kvasil, V.O. Nesterenko, W. Kleinig, and P.-G. Reinhard, Phys. Scr. **89**, 054023 (2014).
29. V.O. Nesterenko, A. Repko, J. Kvasil, and P.-G. Reinhard, Phys. Rev. Lett. **120**, 182501 (2018).
30. V.O. Nesterenko, J. Kvasil, A. Repko, and P.-G. Reinhard, Eur. Phys. J. Web of Conf. **194**, 03005 (2018).
31. A. Repko, J. Kvasil, and V.O. Nesterenko, Phys. Rev. C **99**, 044307 (2019).
32. V.O. Nesterenko, J. Kvasil, and P.-G. Reinhard, Phys. Rev. C **66**, 044307 (2002).
33. V.O. Nesterenko, W. Kleinig, J. Kvasil, P. Vesely, P.-G. Reinhard, and D.S. Dolci, Phys. Rev. C **74**, 064306 (2006).

34. A. Repko, J. Kvasil, V. O. Nesterenko, and P.-G. Reinhard, arXiv:1510.01248[nucl-th].
35. Yoshiko Kanada-En'yo and Yuki Shikata, Phys. Rev. C **95**, 064319 (2017).
36. Yoshiko Kanada-Enyo, Yuki Shikata, and Horiyuki Morita, Phys. Rev. C **97**, 014303 (2018).
37. Yoshiko Kanada-En'yo and Hisashi Horiuchi, Front. Phys. **13**, 132108 (2018).
38. Yuki Shikata, Yoshiko Kanada-En'yo, and Hiroyuki Morita, arXiv:1902.10962 [nucl-th].
39. Yoshiko Kanada-En'yo and Yuki Shikata, arXiv:1903.01075 [nucl-th].
40. J. Endres et al, Phys. Rev. Lett. **105**, 212503 (2010).
41. D. Savran, T.Aumann, and A.Zilges, Prog. Part. Nucl. Phys. **70**, 210 (2013).
42. A. Bracco, E.G. Lanza, and A. Tamii, Prog. Part. Nucl. Phys. **106**, 360 (2019).
43. P.-G. Reinhard and W. Nazarewicz, Phys. Rev. C **87**, 014324 (2013).
44. P. Ring, P. Schuck, *The Nuclear Many-Body Problem* (Springer-Verlag, Berlin, 1980).
45. D. Vautherin, D.M. Brink, Phys. Rev. C **5**, 626 (1972).
46. M. Bender, P.-H. Heenen, P.-G. Reinhard, Rev. Mod. Phys. **75**, 121 (2003).
47. M. Bender, K. Rutz, P.-G. Reinhard, J.A. Maruhn, Eur. Phys. J. A **8**, 59 (2000).
48. P.-G. Reinhard, Ann. Phys. (Leipzig), **504**, 632 (1992).
49. E. Chabanat, P. Bonche, P. Haensel, J. Meyer, and R. Schaeffer, Nucl. Phys. A**635**, 231 (1998).
50. W. Kleinig, V. O. Nesterenko, J. Kvasil, P.-G. Reinhard and P. Vesely, Phys. Rev. C**78**, 044313 (2008).
51. P. Klüpfel, P.-G. Reinhard, T. J. Burvenich, and J. A. Maruhn, Phys. Rev. C**79**, 034310 (2009).
52. J. Bartel, P. Quentin, M. Brack, C. Guet, and H.-B. Haakansson, Nucl. Phys. A**386**, 79 (1982).
53. V. O. Nesterenko, W. Kleinig, J. Kvasil, P. Vesely, and P.-G. Reinhard, Int. J. Mod. Phys. E **17**, 89 (2008).
54. D. G. Ravenhall and J. Wambach, Nucl. Phys. A **475**, 468 (1987).
55. A.M. Krumbholz et al, Phys. Lett. B **744**, 7 (2015).
56. A. Leprêtre, H. Beil, R. Bergère, P. Carlos, A. de Miniac and A. Veyssièrre, Nucl. Phys. A**219**, 39 (1974).
57. J.M. Wyckoff, B. Ziegler, H.W. Koch, and R. Uhlig, Phys. Rev. **137**, B576 (1965).
58. G.J. O' Keefe, M.N. Thompson, Y.I. Assafiri, and R.E. Pywell, Nucl. Phys. A**469**, 239 (1987).
59. S.C. Fultz, B. A. Alvarez, B. L. Berman, and P. Meyer, Phys. Rev. C**10**, 608 (1974).
60. B.S. Ishkhanov, I.M. Kapitonov, I.M. Piskarev, and V.G. Shevchenko, Sov. J. Nucl. Phys. **14**, 16 (1972).
61. V.O. Nesterenko, A. Repko, J. Kvasl, and P.-G. Reinhard, arXiv:1904.08302 [nucl-th].
62. A. Carbone, G. Colo, A. Bracco, L. G. Cao, P. F. Bortignon, F. Camera, and O.Wieland, Phys. Rev. C **81**, 041301(R) (2010).
63. A. Repko and J. Kvasil, arXiv:1904.11259 [nucl-th]; to be published in Proceed. of XXV Nuclear Physics Workshop (Kazimierz Dolny, Poland, 2019).
64. H. Überall, *Electron Scattering from Complex Nuclei*, (Acaemic Press, New York, 1971).
65. J. Heisenberg and H.P. Blok, Ann. Rev. Nucl. Part. Sci. **33**, 569 (1983).
66. C.N. Papanicolas et al, Phys. Rev. Lett. **54**, 26 (1985).
67. D.H. Jakubassa-Amundsen and V.Yu. Ponomarev, Phys. Rev. C**95**, 024310 (2017).
68. J.D. Walecka, *Electron Scattering for Nuclear and Nucleon Structure* (Cambridge Univ. Press, Cambridge, 2004).
69. P. von Neumann-Cosel and A. Tamii, arXiv:1903.11159 [nucl-ex].